COMBINED SYNTHETIC X-RAY AND RADIO OBSERVATIONS OF SIMULATED RADIO JETS

I. L. Tregillis
Los Alamos National Laboratory
Mail Stop B259, Los Alamos, NM 87545, U.S.A.
IANT@LANL.GOV
T. W. Jones, D. Ryu
TWJ@MSI.UMN.EDU, RYU@CANOPUS.CHUNGNAM.AC.KR

Abstract

We present results from an extensive synthetic observation analysis of numerically-simulated radio galaxy jets. This is the first such analysis to be based on simulations with sufficient physical detail to allow the application of standard observational analysis techniques to simulated radio galaxies. Here we focus on extracting magnetic field properties from non-thermal intensity information. We study field values obtained via the combination of synchrotron radio and inverse-Compton X-ray data as well as those from the minimum-energy approach. The combined radio/X-ray technique provides meaningful information about the field. The minimum-energy approach retrieves reasonable field estimates in regions physically close to the minimum-energy partitioning, though the technique is highly susceptible to deviations from the underlying assumptions. We also look at how the two field measurement techniques might be combined to provide a rough measure of the actual energy in particles and fields. A full report on this work can be found in the Astrophysical Journal, Volume 601, page 778.

1 Introduction

X-ray observations of extragalactic radio sources provide a useful complement to detections of radio synchrotron emission. For instance, it has been known for decades that detections of inverse-Compton scattering of the cosmic microwave background (CMB) (hereafter IC/3K emission) can be combined with radio synchrotron observations to extract information about non-thermal particles and magnetic fields in radio galaxies (e.g., Harris & Romanishin, 1974; Cooke, Lawrence, & Perola, 1978; Harris & Grindlay, 1979).

In the absence of complementary X-ray observations, minimum-energy (ME) arguments are often used to estimate field strengths. However, conclusive theoretical arguments for equipartition between radio-emitting electrons and magnetic fields remain elusive.

Both ME and IC/3K field measures require assumptions about the particle and field distributions, such as volume filling factors, spectral cutoffs, and other parameters that are not directly accessible to observations. Customary assumptions include a uniform magnetic field geometry and a pure power-law distribution of particles. Often, however, such assumptions may be unrealistic.

Here we use synthetic observations as a tool for investigating these issues in a manner that makes minimal use of simplifying assumptions, while retaining the benefit of complete knowledge of the actual physical conditions being observed. We present the highlights of this investigation here; a full report can be found in Tregillis, Jones, & Ryu (2004) (hereafter TJR04).

2 Numerical methods

Our numerical methods have been detailed in Jones, Ryu, & Engel (1999), Tregillis, Jones, & Ryu (2001), and TJR04. We refer the reader to those papers for a complete description. In short, we follow the bulk flow through a three-dimensional total variation diminishing (TVD) Eulerian ideal magneto-hydrodynamic (MHD) scheme. Within the non-relativistic bulk MHD flows, we evolve a passive population of relativistic electrons ($E_e \leq 10$ GeV) through the standard particle kinetic equation. The particle evolution is treated self-

Table 1: Summary of simulations

Model	ϵ	B_{xo} (μG)	$\tau_{\rm rad}/\tau_{\rm end}$
Control (1)	0.0	0.39	1.6×10^3
Injection (2)	10^{-4}	0.39	1.6×10^3
Cooling (3)	0.0	5.7	1.0

consistently, incorporating first-order Fermi acceleration at shocks as well as adiabatic and radiative cooling.

2.1 The models

The passive nature of the non-thermal electron populations enabled us to conduct several numerical simulations of the same dynamically-identical jet, each focused on a different set of cosmic ray (CR) parameters. The dynamical model consisted of a light ($\rho_{\rm jet}/\rho_{\rm amb}$ = 10^{-2}), supersonic ($\mathcal{M}_{\rm jet}$ = 8), magnetized (B_ϕ = $2B_{x0}(r/r_j)$ for $r \le r_j$) jet propagating through a uniform ambient magnetized medium ($B_{\rm amb} = B_x = B_{x0}$). The jet was not magnetically dominated, with $\beta = 10^2$ initially on axis.

Radiative cooling timescales ($\tau_{\rm rad}$) were parameterized through the physical value of B_{x0}. The injection of fresh non-thermal particles at shocks was parameterized via the parameter ϵ, the fraction of the thermal flux through each shock injected into the downstream non-thermal population. Parameter values for all three models are listed in Table 1.

In each model, the jet non-thermal electron population entered with a momentum index q = 4.4, representing a synchrotron spectral index, $\alpha = (q-3)/2 = 0.7$, where $S_\nu \propto \nu^{-\alpha}$.

2.2 Synthetic observations

We construct synthetic observations of the simulated jets in the following manner. First, we combine vector magnetic field and non-thermal electron distribution data to calculate self-consistent synchrotron radio and IC/3K X-ray volume emissivities in every zone of the computational grid. Then we apply a ray-casting procedure to perform line-of-sight (LOS) integrations and project the simulated objects on the sky. The output data is written in FITS format and analyzed using conventional packages (`MIRIAD` and `KARMA` (Gooch, 1995)).

As given by Jones, O'Dell, & Stein (1974), the synchrotron emissivity is

$$j_s(\nu) = j_{\alpha 0}\frac{4\pi e^2}{c} f(p_s) p_s^q \left(\frac{\nu_{B_\perp}}{\nu}\right)^\alpha \nu_{B_\perp}. \quad (1)$$

The spectral index α is related to the local electron momentum index q via α = $(q-3)/2$, $\nu_{B_\perp} = eB\sin\Omega/(2\pi m_e c)$, where Ω projects the local field onto the sky, and $j_{\alpha 0}$ is an order-unity dimensionless constant, defined in Jones, O'Dell, & Stein (1974). For a selected observing frequency, ν, the distribution, $f(p_s)$, and the index, q, are determined for each point on the grid by establishing the relevant electron momentum from the relation $p_s = [2\nu/(3\nu_{B_\perp})]^{(1/2)}$, with p_s in units $m_e c$. This calculation properly accounts for spectral curvature and the orientation of the magnetic field on the plane of the sky.

The X-ray IC/3K emissivity, $j_{\rm 3K}(\nu_X)$, can be sim-

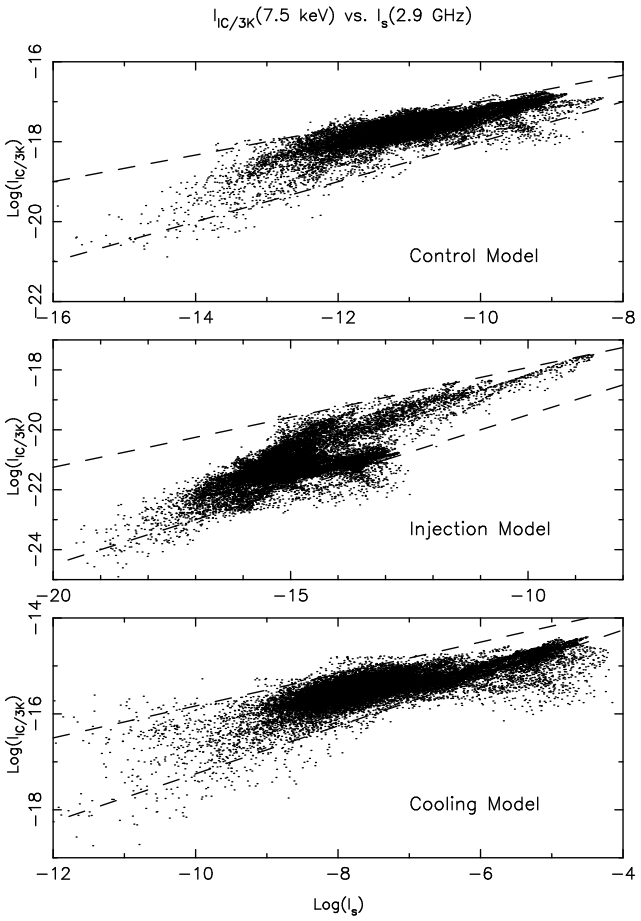

Figure 1: Scatter plots of 7.5 keV IC/3K versus 2.9 GHz synchrotron brightness in code units. The dashed lines represent the relationships $I_{\rm IC/3K} \propto I_S^{1/3}$ and $I_{\rm IC/3K} \propto I_S^{1/2}$. They are solely for comparison and are not statistical fits. From TJR04.

ply expressed at a selected X-ray frequency, ν_X, in terms of the synchrotron emissivity, $j_s(\nu_X)$, in Eq. (1) extrapolated to ν_X; namely (Jones, O'Dell, & Stein, 1974)

$$j_{3\rm K}(\nu_X) = e^{3\rm K}_{\alpha 0}\ \frac{\sigma_T c}{e^2}\ \frac{c u_\mu \nu_\mu^{\alpha-1}}{4\pi \nu_{B_\perp}^{1+\alpha}}\ (1+z)^{3+\alpha}\ j_s(\nu_X), \tag{2}$$

where $u_\mu = aT_0^4$ and $\nu_\mu = kT_0/h$ are the energy density and characteristic frequency, respectively, at the current epoch of the CMB, while $e^{3\rm K}_{\alpha 0}$ is another order-unity constant that can be obtained from Jones, O'Dell, & Stein (1974). We note in Eq. (2) that $j_s(\nu_X)$ is normalized and α is determined at $p_\mu = (\nu_X/\nu_\mu)^{1/2}$.

3 Radio and X-ray brightness correlations

Correlations between different intensity distributions accurately reflect basic dynamical relationships between particles and fields in our models. Figure 1 depicts 7.5 keV IC/3K X-ray brightness plotted against 2.9 GHz radio synchrotron brightness for all three models.

The IC/3K versus radio trends are well-described for all three models by the proportionality $I_{\rm IC/3K} \propto I_S^m$, with $m \approx$ 1/3–1/2. If the magnetic field scaled with the electron density as $B \propto n_e^b$, then since $I_{\rm IC/3K} \propto n_e \mathcal{D}$ and $I_S \propto n_e \mathcal{D}\ B^{1+\alpha}$ (where $\mathcal{D}$ is the path length) we would have $I_{\rm IC/3K} \propto I_S^{1/(1+b(1+\alpha))} \equiv I_S^m$.

On the other hand, standard arguments suggest $B \propto \rho^{2/3}$ for a disordered field in compression-dominated flows. Assuming $n_e \propto \rho$, this gives m = 3/(5 + 2α). For $\alpha \sim$ 0.5–1, typical of the synthetic radio sources, this would yield $m \sim$ 0.5–0.43. Alternatively, at perpendicular shocks one expects $B \propto \rho$, resulting in m = 1/(2 + α), or $m \sim$ 0.4–0.33. Thus, the observed trends are consistent with field evolution dominated by these dynamical processes. Field evolution controlled by flux tube stretching would satisfy $B \propto \ell$, where ℓ is the length of the flux tube (e.g., Gregori et al., 2000). In this case there is no explicit interdependence between density and magnetic field. We know that the magnetic fields in the simulated object are filamented, so flux tube stretching certainly takes place. The above exercise brings out the fact that the global field evolution in the simulated object is dominated by compression, however. This matches our conclusions about the simulated field behaviors in Tregillis, Jones, & Ryu (2001). Sheared field evolution, while clearly involved and locally important, predominantly adds scatter to the correlations in Fig. 1.

Similar insights and information about the intensity of the omni-directional synchrotron flux can be obtained from plots of the synchrotron self-Compton (SSC) X-ray brightness versus the radio brightness, and SSC versus IC/3K brightness.

4 Estimating field strengths

Magnetic field strength can be calculated very simply from synchrotron and IC/3K intensities for a uniform medium when the electron distribution is a power-law. We used the following expression for this estimated field, B_{ic} in μG (e.g., Jones, O'Dell, & Stein, 1974; Harris & Romanishin, 1974; Harris & Grindlay, 1979):

$$B_{ic}^{1+\alpha} = (1.06\times10^{-11})\ (2.09\times10^4)^{\alpha-1} \left(\frac{j^{3\rm K}_{\alpha 0}}{j_{\alpha 0}}\right) \times (1+z)^{3+\alpha}\ \left(\frac{\nu_r}{\nu_X}\right)^\alpha \frac{I_S(\nu_r)}{I_{\rm IC/3K}(\nu_X)}. \tag{3}$$

For uniform particle and field distributions, this expression is exactly equivalent to inverting the analytic calculation of synchrotron and IC/3K surface brightnesses in our synthetic observations.

Similarly, the standard expression used to compute the minimum-energy magnetic field, B_{me}, in Gauss is (Miley (1980)):

$$B_{me} = 5.69\times10^{-5} \left[\frac{\nu_2^{1/2-\alpha} - \nu_1^{1/2-\alpha}}{(1/2-\alpha)}\right]^{2/7} \times \left[\left(\frac{1+k}{\eta}\right) \frac{F(\nu_r)}{\nu_r^{-\alpha}} \frac{(1+z)^{3+\alpha}}{\theta_x\ \theta_y\ \ell\ \sin^{3/2}\vartheta}\right]^{2/7}. \tag{4}$$

Here $F(\nu_r)$ is the observed radio flux density within an observing beam, $k \equiv U_{\rm proton}/U_E$, η is a magnetic field volume filling factor, ϑ is the angle between the magnetic field and the line of sight, θ_x and θ_y are the semi-major and semi-minor axes of the observing beam in arcseconds, ℓ is the path length through the source in kpc, and ν_1 and ν_2 are the *fixed* lower and upper synchrotron cutoff frequencies in the source frame, expressed in GHz. We assume below for simplicity that $k = \eta = \sin\vartheta$ = 1. The magnetic field is so tangled and intermittent that assuming $\sin\vartheta$ = 1 introduces errors of only a few percent into our analysis.

In order to incorporate the full non-thermal electron distributions as well as possible into B_{me}, the frequency limits needed in equation (4) correspond in

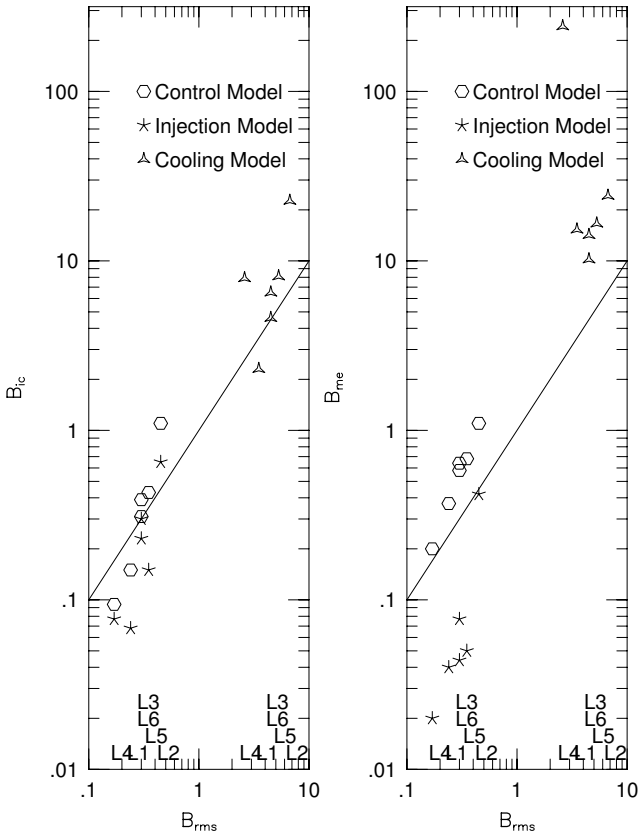

Figure 2: Comparisons of magnetic field measures. Symbols indicate the electron transport model. Associated line-of-sight numbers are marked at the bottom of each plot according to the associated $B_{\rm rms}$ values. From TJR04.

each model to the characteristic synchrotron frequencies of the lowest and highest energy electrons and the fiducial magnetic field for each model. Those turn out to be ν_1 = 100 Hz and ν_2 = 30 GHz for the Control and Injection models; for the Cooling model, ν_1 = 1500 Hz and ν_2 = 450 GHz. Our conclusions do not depend on any of these parameter choices.

Our analysis is summarized in Fig. 2, which compares B_{ic} and B_{me} to $B_{\rm rms}$ for the same six LOS in each model. The LOS were chosen to sample a variety of physical and spectral structures within the simulated objects, including jet, hotspot, and lobe structures. Here we comment on the most salient features.

Both empirical field estimates correlate roughly with $B_{\rm rms}$ along the selected lines of sight. The bolometric synchrotron intensity does depend on the rms magnetic field along the line of sight, of course. The spectral emissivity $j_s(\nu) \propto B^{1+\alpha}$, is similar, since in our sources spectral index values in the range $\alpha \sim 0.7$–1 are common. Still it is not obvious a priori how well such a simple measure as $B_{\rm rms}$ should compare to inferred values, so the experiment is valuable. Two-thirds of the B_{ic} (B_{me}) points are within a factor of two (three) of $B_{\rm rms}$. The B_{ic} values are approximately randomly distributed with respect to $B_{\rm rms}$.

LOS 6 passes through the jet near its origin. At that location, the field structure is relatively simple and approximates that introduced at the computational boundary. Furthermore, the emission is dominated by young electron populations in the jet that have not yet been subjected to strong radiative aging. For all three models B_{ic} is very close to $B_{\rm rms}$ as well as the projected axial base jet magnetic field in the simulation.

Values of B_{ic} for lobe LOS (e.g., LOS 1 and 4) tend to fall below $B_{\rm rms}$. This bias results from the presence of substantial electron populations in weak field regions that contribute little to the radio emission, but that do produce X-rays. In effect the IC/3K intensity provides an overestimate of the number of radio emitting electrons, so that under the uniform source hypothesis the field apparently needed to account for the radio emissions is weakened. When compared to the distribution of field values along individual LOS, we find B_{ic} to be generally representative of the values being sampled. Thus it does give a "meaningful" result, if not a simply defined quantitative one.

Notable exceptions occur in the presence of strong spectral curvature, such as along LOS 4 in the cooling model. Intentionally, no correction was made for the convex spectrum at this location, in order to expose its potential influence. The 1.2 keV IC/3K emission used to compute B_{ic} comes from 1 GeV electrons, while the 2.9 GHz emission is produced by electrons with energies about an order of magnitude higher, even in the strongest field regions along this LOS. With a convex electron spectrum the computed B_{ic} will be artificially increased, as simple arguments can show. Suppose, for example, we measured the bolometric synchrotron intensity, I_S, from electrons of energy γ_S and the bolometric IC/3K intensity, $I_{\rm 3K}$, from electrons of energy $\gamma_{\rm 3K}$. If the object were homogeneous, and we fixed the observed radio band, it is simple to show that $B \propto (I_S/I_{\rm 3K}) N_{\gamma_{\rm 3K}}/N_{\gamma_S}$, where $N_{\gamma_{\rm 3K}}$ and N_{γ_S} represent the number of electrons required to produce the observed intensities. If we assumed that $N_{\gamma_{\rm 3K}}$ and N_{γ_S} were connected by a powerlaw in γ with the powerlaw index determined by the high energy electrons responsible for the radio band, but the distribution is actually

convex, we would always overestimate B, since we would overestimate $N_{\gamma_{3K}}/N_{\gamma_S}$. This same influence has an even more striking impact on the value of B_{me} for LOS 4 in the cooling model. Under the equipartition that accompanies the minimum energy assumption, the effective overestimate of the electron population also exaggerates the estimated magnetic field energy, leading to a field value about two orders of magnitude greater than $B_{\rm rms}$ and even an order of magnitude greater than $B_{\rm max}$ along this LOS.

Our simulated objects are not in electron/magnetic field energy equipartition, nor is there physics in the simulations expected to produce this kind of equipartition. Thus, while B_{ic} values are largely randomly distributed with respect to $B_{\rm rms}$, there are obvious biases in the relationship between B_{me} and $B_{\rm rms}$. Those biases correctly reflect actual deviations from the minimum energy condition. In short, they trace the relationship between non-thermal particle and magnetic field energies in the predominant emission regions.

LOS 2 passes through a hotspot resulting from a shock produced as the jet impinges on the near boundary of its cocoon. The magnetic field is relatively compressed and organized there, making the LOS distribution sharply peaked. Virtually all of the radio emission in this direction originates in the hotspot, so that the B_{ic} and B_{me} values for all three models lie close to $B_{\rm rms}$. This is the only LOS we sampled that returns a B_{me} estimate in the injection model that is close to $B_{\rm rms}$. It is, in fact, the only LOS we sampled that has emissions in that electron transport model predominantly from regions close to electron/magnetic field equipartition.

5 Estimating energy partitioning

In the previous section we found that the minimum energy magnetic fields were close to the RMS fields (or any other simple statistical measure) only when the emission was dominated by relativistic plasma close to equipartition. Interestingly, however, biases in B_{me} correctly reflected the degree of deviation from equipartition of the dominant plasma, consistent with whether more energy was stored in particles or fields. This is encouraging, as it demonstrates that biases in B_{me} contain useful information about the partitioning even when the source plasma is not in a minimum-energy configuration. In practice, unfortunately, when we lack a reliable fiducial field measure, we have no way to gauge biasing in the minimum-energy values.

On the other hand, we also found that a synchrotron/inverse-Compton analysis provides reasonable estimates of characteristic magnetic fields, in particular $B_{\rm rms}$, in our simulated objects. While there are biases that can degrade the estimates when the fields are significantly more intermittent than the non-thermal electrons or when the electron energy spectra are strongly aged, the B_{ic} values we derived were mostly within a factor of two of the RMS fields.

This all suggests that combining B_{ic} and B_{me} might reveal a meaningful estimate of the ratio of non-thermal electron and magnetic field energy and, consequently, provide an improved estimate of the total non-thermal energy compared to the minimum energy.

The obvious parameter for comparing magnetic and non-thermal particle energies is the ratio of their local densities; namely,

$$d \equiv \frac{U_B}{U_E}. \tag{5}$$

Standard expressions for the minimum-energy magnetic field, B_{me}, (i.e., assuming a uniform source, a power-law $f(p)$, and a fixed frequency band) (see Eq. (4)), lead to the simple relation

$$d = d_{\rm min}\left(\frac{B}{B_{me}}\right)^{7/2}. \tag{6}$$

Here B is the actual field strength, B_{me} is the field strength inferred from the observed synchrotron emission, and $d_{\rm min} \equiv \frac{3}{4}(1+k)$ corresponds to the case $B = B_{me}$. The exact value of k makes no substantial difference to our conclusions, so for convenience we will still apply the commonly used value $k = 1$. Similar expressions for the total energy density in non-thermal particles and magnetic fields can also be derived.

Since B_{ic} provides meaningful information about the magnetic field, it seems reasonable to use B_{ic} for B in Eq. (6). Doing so leads to an observational measurement of the partitioning parameter, d. In the case of power-law spectra and uniform fields (again, the standard assumptions underlying the B_{me} and B_{ic} derivations), this measurement will exactly reproduce the true partitioning.

In practice, any source will deviate from those oversimplified conditions, as do our models. Since d varies faster than the cube of the inferred magnetic field, small errors in the measurement of the local field may

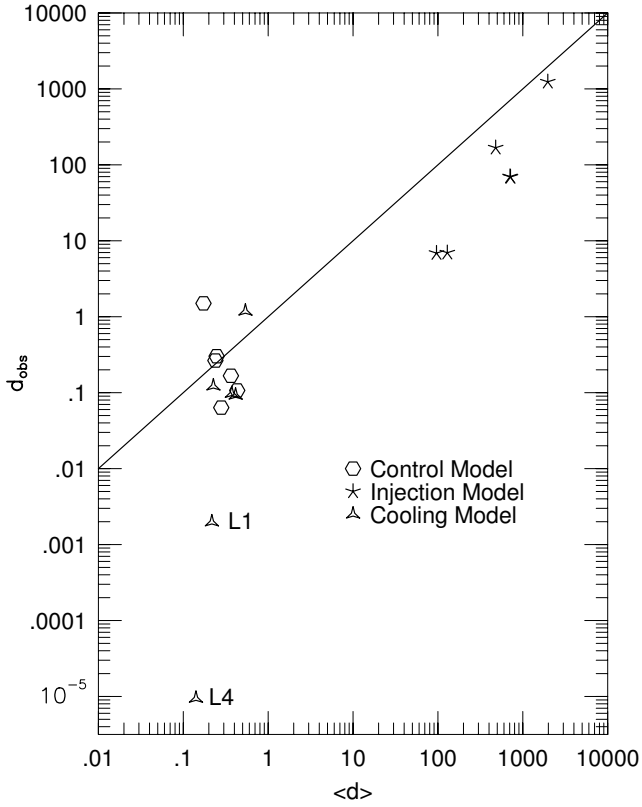

Figure 3: Comparisons of $d_{\rm obs}$ and $\langle d \rangle$. Symbols indicate the electron transport model. From TJR04.

grow quickly into large errors in d. Thus it is worth using synthetic observations to investigate the utility of this approach.

As mentioned in section 4, LOS 6 passes through the base of the jet. Physical conditions near the base of the jet should be close to those set by the simulation initial conditions. Furthermore, the jet magnetic field is smoothly helical as it enters the grid, and thus more ordered there than throughout the rest of the source. This LOS therefore provides a useful test of the observationally-derived d value. Table 2 lists the d values at the base of the jet defined by initial conditions in all three models, and the observationally derived values.

Table 2: Energy partitioning at the jet base

d	Control	Injection	Cooling
Defined	1.6×10^{-1}	1.6×10^{3}	1.6×10^{-1}
Derived	1.7×10^{-1}	1.2×10^{3}	9.2×10^{-2}

For k = 1 ($d_{\rm min}$ = 1.5), the control and cooling model jets enter the computational grid within an order of magnitude of the minimum-energy partitioning. The injection model jet is several orders of magnitude out of equipartition, with the dominant contribution coming from the field. We see that in all three models, the observationally derived value of d matches the value set by initial conditions to well within a factor of two.

Encouraged by this result, we cast our net more widely, using our privileged information as simulationists to compute $\langle d \rangle$, the mean value of d along each line of sight, in all three models. Figure 3 shows the observationally derived partitioning value $d_{\rm obs}$ plotted against $\langle d \rangle$. There is a rough correspondence between $d_{\rm obs}$ and $\langle d \rangle$ for most of the data, although the agreement is not generally better than about an order of magnitude. Though we should not expect exact correspondence, since $d_{\rm obs}$ is based on two indirect measures weighted to different points along each LOS. Two LOS in the cooling model (label L1 and L4 on Fig. 3) show strong deviation from the mean d value. Both of those cases are due to spectral curvature in the lobe, against which we have not corrected this simple experiment. If the electron spectrum is convex, care must be taken to properly account for the low-energy electrons, or B_{me} will be overestimated, which in turn will have a strong influence on $d_{\rm obs}$.

The estimation of local energy partitioning based on B_{ic} and B_{me} works best in regions that are not strongly radiatively aged and where the partitioning is not expected to vary strongly over short distances, such as inside jet structures. There is increasing evidence for Doppler-boosted IC/3K emission from some radio jets (Tavecchio et al., 2000; Sambruna et al., 2001; Celotti et al., 2001). It would be interesting to apply a relativistic version of this technique to those sources, properly accounting for beaming effects.

Acknowledgments

We would like to thank the sponsors and organizers of "X-Ray and Radio Connections" for putting together a lively and enjoyable meeting.

References

Celotti, A., Ghisellini, G., Chiaberge, M. 2001, MNRAS, 321, L1

Cooke, B. A., Lawrence, A., Perola, G. C. 1978, MNRAS, 182, 661

Gooch, R. E. 1995, in ASP Conf. Ser. 101, Astronomical Data Analysis Software and Systems V, ed. G.

H. Jacoby & J. Barnes (San Francisco: ASP), 80
Gregori, G., Miniati, F., Ryu, D., Jones, T. W. 2000, ApJ, 543, 775
Harris, D. E., Grindlay, J. E. 1979, MNRAS, 188, 25
Harris, D. E., Romanishin, W. 1974, ApJ, 188, 209
Jones, T. W., O'Dell, S. L., Stein, W. A. 1974, ApJ, 188, 353
Jones, T. W., Ryu, D., Engel, A. 1999, ApJ, 512, 105
Miley, G. 1980, ARA&A, Vol. 18 (Annual Reviews, Inc.), 165
Sambruna, R. M., Urry, C. M., Tavecchio, F., Maraschi, L., Scarpa, R., Chartas, G., Muxlow, T. 2001, ApJ, 549, L161
Tavecchio, F., Maraschi, L., Sambruna, R. M., Urry, C. M. 2000, ApJ, 544, L23
Tregillis, I. L., Jones, T. W., Ryu, D. 2001, ApJ, 557, 475
—. 2004, ApJ, 601, 778 (TJR04)